Nano Research 2017, 10(8): 2599–2609
DOI 10.1007/s12274-017-1462-1
Research Article
ISSN 1998-0124
CN 11-5974/O4

Enhanced electrocatalytic activity of Co@N-doped carbon nanotubes by ultrasmall defect-rich TiO_2 nanoparticles for hydrogen evolution reaction

Jiayuan Yu[1,2], Weijia Zhou[1] (✉), Tanli Xiong[1], Aili Wang[1,2], Shaowei Chen[1,3], and Benli Chu[2]

[1] *School of Environment and Energy, Guangdong Provincial Key Laboratory of Atmospheric Environment and Pollution Control, South China University of Technology, Guangzhou Higher Education Mega Center, Guangzhou 510006, China*
[2] *School of Physics and Telecommunication Engineering, South China Normal University, Guangzhou Higher Education Mega Center, Guangzhou 510006, China*
[3] *Department of Chemistry and Biochemistry, University of California, 1156 High Street, Santa Cruz, CA 95064, USA*

Received: 11 December 2016
Revised: 29 December 2016
Accepted: 1 January 2017

KEYWORDS
ultrasmall nanoparticle, TiO_2, defect structure, carbon nanotube, hydrogen-evolution reaction

ABSTRACT

Despite being technically possible, splitting water to generate hydrogen is practically unfeasible, mainly because of the lack of sustainable and efficient earth-abundant catalysts for the hydrogen-evolution reaction (HER). Herein, we report a durable and highly active electrochemical HER catalyst based on defect-rich TiO_2 nanoparticles loaded on Co nanoparticles@N-doped carbon nanotubes (D-TiO_2/Co@NCT) synthesized by electrostatic spinning and a subsequent calcining process. The ultrasmall TiO_2 nanoparticles are 1.5–2 nm in size and have a defect-rich structure of oxygen vacancies. D-TiO_2/Co@NCT exhibits excellent HER catalytic activity in an acidic electrolyte (0.5 M H_2SO_4), with a low onset potential of −57.5 mV (1 mA·cm^{-2}), a small Tafel slope of 73.5 mV·dec^{-1}, and extraordinary long-term durability. X-ray photoelectron spectroscopy, electron paramagnetic resonance spectroscopy, and theoretical calculations confirm that the Ti^{3+} defect-rich structure can effectively regulate the catalytic activity for electrochemical water splitting.

1 Introduction

Hydrogen is considered as one of the promising alternatives for replacing fossil fuels owing to its high energy density and eco-friendliness. Electrochemical water splitting is a clean and efficient method for producing a large quantity of molecular hydrogen [1–3]. To date, platinum-based materials are the most efficient catalysts for the hydrogen-evolution reaction (HER), but their high cost and low abundance significantly hamper their widespread applications [4, 5]. Thus, considerable efforts have been directed towards the development of low-cost and earth-abundant catalysts to replace platinum-based catalysts

Address correspondence to eszhouwj@scut.edu.cn

[6]. In the past decade, transition-metal carbides [7], sulfides [8–11], and phosphides [12–14] have been intensively investigated as HER catalysts. In addition, recent studies have shown that the active metal@carbon materials (e.g., cobalt, iron, chromium, and gold) are a family of efficient hydrogen-evolving catalysts [15, 16]. For example, wrapping CoNi metal particles with ultrathin graphene layers significantly promoted the electron penetration and enhanced the catalytic activity for the HER [17]. The catalytically active sites are mainly located at the carbon atoms, and their electronic state density can be modulated by the adjacent transition-metal elements [18].

Titanium dioxide (TiO_2), which is one of the best-known semiconductor photocatalysts, has been intensively investigated for environmental-pollutant elimination and photocatalytic hydrogen production [19–21]. In addition, TiO_2 played a key role as an oxide support in enhancing the catalytic activity of oxide-supported catalysts via strong metal-support interaction (SMSI) [22–24]. For example, Fu and Zheng atomically dispersed palladium catalysts on the surface of TiO_2, which substantially enhanced the catalytic activity of palladium for the generation of hydrogen through the water–gas-shift reaction [22]. Notably, a defective structure in TiO_2 nanoparticles can enhance the activities of various catalytic reactions [25, 26], such as the oxygen-reduction reaction [27, 28]. However, this has rarely been reported for electrochemical water splitting [29]. The design of structural defects in electrocatalysts is a scalable method for exposing active edge sites and improving the HER activity [2, 10, 30–32]. In this study, ultrasmall, defect-rich TiO_2 nanoparticles loaded on Co nanoparticles@N-doped carbon nanotubes (D-TiO_2/Co@NCT) were synthesized by electrostatic spinning and a subsequent calcining process. The defect-rich structure in the ultrasmall TiO_2 nanoparticles effectively enhanced the HER activity of the Co@NCT, which was confirmed by X-ray photoelectron spectroscopy (XPS), electron paramagnetic resonance (EPR) spectroscopy, and theoretical calculations. The obtained D-TiO_2/Co@NCT exhibited excellent HER catalytic activity in an acidic electrolyte (0.5 M H_2SO_4), with a low onset potential of −57.5 mV (1 mA·cm^{-2}), a small Tafel slope of 73.5 mV·dec^{-1}, and extraordinary long-term durability.

2 Experimental

2.1 Synthesis of D-TiO_2/Co@NCT

Chemicals: All reagents were of analytical grade and used without further purification. Poly (vinylpyrrolidone) (PVP) powder (molecular weight = 1,300,000–1,500,000 g·mol^{-1}), cobalt acetate ($C_2H_3CoO_2$), cyanamide ($C_2H_4N_4$), tetra-n-butyl titanate ($Ti(OC_4H_9)_4$), ethanol (C_2H_5OH), acetic acid (CH_3COOH), sulfuric acid (H_2SO_4), hydrochloric acid (HCl), and 20 wt.% Pt/C were purchased from Sinopharm Chemical Reagents Beijing Co.

The synthesis procedure was as follows. First, 5 g PVP was added to a mixture of 20 mL of ethanol and 15 mL of acetic acid in a capped bottle. The obtained solution was stirred vigorously for 6 h to ensure complete solubility. Then, 3.4 g of $Ti(OC_4H_9)_4$ was added to the mixture, and the stirring was continued until the polymer solution became clear. Next, 2.49 g of $C_2H_3CoO_2$ was added to the solution, and the mixture was continuously stirred for another 6 h. In a typical electrospinning process, the resulting precursor solution was loaded into a 5-mL plastic syringe with a stainless-steel needle. The distance between the needle tip and the collector was ~15 cm. The needle tube was connected to an applied voltage of 15 kV. The as-electrospun Co-Ti-PVP fibers were collected on the aluminum foil and then dried at 60 ℃ in vacuum for 24 h. The dried samples of Co-Ti-PVP fibers (100 mg) were placed in the middle of a large crucible, and 100 mg of cyanamide powder was placed in the upstream zone of a small crucible. Then, the small crucible was loaded into the large-crucible reactor, which was placed in a horizontal tube furnace and connected to a gas feed system. The furnace was heated at 450 ℃ for 2 h and then at 750 ℃ for 2 h in an argon atmosphere. The black products (denoted as D-TiO_2/Co@NCT) were then washed with a 1 M HCl aqueous solution to remove the unwrapped Co particles. For comparison, blank samples were also synthesized by similar procedures but without the addition of $C_2H_3CoO_2$ or $Ti(OC_4H_9)_4$, which are denoted as TiO_2-NC and Co@NCT, respectively.

2.2 Characterization

The morphologies of the obtained samples were

characterized by field-emission scanning electron microscopy (FESEM, Model JSM-760F). Transmission electron microscopy (TEM) was performed using a JOEL JEM 2100F microscope. Powder X-ray diffraction (XRD) patterns of the samples were recorded using a Bruke D8 Advance powder X-ray diffractometer with Cu Kα (λ = 0.15406 nm) radiation. XPS was performed using a PHI X-tools instrument (ULVAC-PHI). The possible intrinsic defects in TiO_2 were identified via EPR spectroscopy using a Bruker E500 spectrometer operating at 9.86698 GHz, at room temperature. The Brunauer–Emmett–Teller (BET) surface area was determined using Micromeritics ASAP 2010 with nitrogen adsorption at 77 K, as well as the Barrett–Joyner–Halenda method.

2.3 Electrochemistry

Electrochemical measurements were performed using an electrochemical workstation (CHI 760E; CH Instruments, Inc.) in a 0.5 M H_2SO_4 aqueous solution. A saturated calomel electrode (Hg/Hg_2Cl_2 in a saturated KCl solution) and carbon cloth (1 cm × 2 cm) were used as the reference and counter electrode, respectively. Next, 5 mg of the catalyst powder was dispersed in a mixed solvent of water/ethanol (1 mL of 1:1 v/v), along with 50 μL of a Nafion solution, under sonication for 30 min. Then, 5 μL of the resulting solution was drop-cast onto a glassy carbon (GC) disk electrode (3 mm in diameter) with catalyst loading of 0.357 mg·cm^{-2} and dried at room temperature. Prior to electrochemical testing, the electrodes were soaked in 0.5 M H_2SO_4 overnight and then activated by a few cyclic-voltammetry (CV) curves to obtain a stable catalytic current. Polarization curves were recorded by sweeping the potential from 0 to −0.6 V (vs. reversible hydrogen electrode (RHE)) at a potential sweep rate of 5 mV·s^{-1} under illumination and in the dark, respectively. A xenon lamp with a light intensity of 100 mW·cm^{-2} was employed as the light source. Electrochemical impedance spectroscopy (EIS) was performed with an amplitude of 10 mV and a frequency range of 100 kHz to 0.01 Hz. The main arc in the EIS spectra was fitted using a simplified Randles equivalent circuit, which consisted of a resistance (R_s), a charge-transfer resistance (R_{ct}, interface electrocatalytic reaction between the electrode and electrolyte) and a constant-phase element, and the fitting parameters were estimated using the Levenberg–Marquardt minimization procedure. CV was used to probe the electrochemical double layer capacitance at nonfaradaic potentials for estimating the effective electrode surface area. The current–time responses were monitored by chronoamperometric measurements for 10 h at an applied potential of −0.15 V (vs. RHE). The gas-production rate was quantified by gas chromatography (GC-2060F; LuNan Analytical Instruments, Ltd.; China).

2.4 Density functional theory (DFT) calculations

All calculations were performed within the framework of DFT, as implemented in the Vienna *Ab initio* Simulation Package [33]. The exchange–correlation interactions were treated using the generalized gradient approximation parameterized by Perdew, Burke, and Ernzerhof [34]. The interaction between ions and electrons was described using the projected augmented wave [35]. The periodic unit was optimized by the conjugate gradient algorithm with an energy cutoff of 400 eV until the force acting on each atom was less than 0.02 eV·Å^{-1}. The Brillouin zone was meshed by the Γ-centered Monkhorst–Pack method with 1 × 4 × 5 k-points for geometry optimizations and the static total energy calculations.

The hydrogen-adsorption Gibbs free energies, ΔG_H, were determined in the same way as in previous studies. The adsorption energy is defined as

$$\Delta E_H = E(TiO_2{+}H) - E(TiO_2) - \tfrac{1}{2} E(H_2) \quad (1)$$

where TiO_2 + H refers to the hydrogen adsorbed on the TiO_2 surface, TiO_2 refers to a clean TiO_2 surface, and H_2 refers to a gas-phase hydrogen molecule. The total energy of H_2 was −6.7 eV in this work, and the hydrogen-adsorption Gibbs free energy (ΔG_H) was calculated as

$$\Delta G_H = \Delta E_H + \Delta E_{ZPE} - T\Delta S \quad (2)$$

where ΔE_H is the hydrogen adsorption energy, ΔE_{ZPE} is the difference in the zero-point energy, T is the temperature (300 K), and ΔS is the difference in entropy between hydrogen that is adsorbed and in the gas phase at 101,325 Pa. A normal-mode analysis was

performed to determine the vibrational frequencies of the adsorbed species, which were used to determine the zero-point energy correction and the entropy. Here, we used 0.24 eV as the correction of ΔE_{ZPE} and $T\Delta S$. Thus, we obtained the following formula for the Gibbs free energy: $\Delta G_H = \Delta E_H + 0.24$ eV [36]. DFT calculation usually employs simplified and computable models from an experiment (dozens of atoms) and cannot fully reproduce the real experiment, because the quantity of data is too large (hundreds of millions of atoms).

3 Results and discussion

The synthesis procedure for D-TiO_2/Co@NCT is illustrated in Fig. 1, and the corresponding morphologies were characterized by FESEM. The Co-Ti-PVP fibers were first synthesized by electrostatic spinning (Fig. S1(a) in the Electronic Supplementary Material (ESM)), which was beneficial for the production of the dispersed CNTs via the subsequent calcining process in an argon atmosphere at 750 ℃ (Fig. 1(a)). Without the electrostatic-spinning process, the precursor of Co-Ti-PVP calcined under the same conditions yielded an amorphous block with sparse CNTs (Fig. S2 in the ESM).

The synthesized D-TiO_2/Co@NCT had a nanotube morphology with a diameter of 15–30 nm and a length of 10–15 μm (Figs. 2(a) and 2(b)), which are similar to those of Co@NCT (Fig. 2(c)). D-TiO_2 nanoparticles were not observed on the surface of the CNTs, owing to their ultrasmall size. The transition metals (such as cobalt, nickel, and iron) catalytically synthesized the CNTs, which is consistent with previous results [15, 37, 38]. In contrast, the calcination of Ti-PVP fibers without cobalt yielded only TiO_2 nanoparticles 100–200 nm in size embedded in porous carbon (TiO_2-NC, Fig. 2(d)). The Co nanoparticles@CNTs were crucial for the synthesis of the ultrasmall TiO_2 nanoparticles, which played an important role in enhancing the catalytic activity of the hydrogen production (Fig. 1(b)).

XRD measurements in Fig. 2(e) showed a broad peak at 25.5° for all samples, corresponding to the graphene (002) crystal planes. For Co@NCT and D-TiO_2/Co@NCT, the peak at 44.2° was consistent with the (111) crystal planes of metal cobalt (JCPDS No. 15-0806). Compared with Co@NCT, in addition to the characteristic peaks of carbon and cobalt, weak peaks at 27.4°, 36.1°, and 54.3° were observed in the D-TiO_2/Co@NCT, which correspond to the (110), (101), and (211) planes, respectively, of rutile TiO_2 (JCPDS No. 21-1276). However, the peak intensities of TiO_2 in the D-TiO_2/Co@NCT were far weaker than those of TiO_2-NC. Nitrogen adsorption/desorption isotherms of the Co@NCT, D-TiO_2/Co@NCT, and TiO_2-NC showed typical type-IV curves with an H_2-type hysteresis loop, indicating the formation of a mesoporous structure. The D-TiO_2/Co@NCT had a far larger BET surface area (139.2 $m^2 \cdot g^{-1}$) than the Co@NCT (40.8 $m^2 \cdot g^{-1}$) and TiO_2-NC (9.6 $m^2 \cdot g^{-1}$) (Fig. 2(f)). This is because of the successful formation of CNTs and ultrasmall TiO_2 nanoparticles (Fig. 3).

The typical TEM images revealed that the overall appearance was CNTs with diameters of 15–30 nm and a wall thickness of 2–8 nm (Figs. 3(a) and 3(b)). Relatively fewer and larger nanoparticles 15–20 nm in size coated by a carbon shell were observed at the end of the CNTs, which had a lattice fringe of 0.206 nm, corresponding to the (111) plane of cobalt (Fig. 3(b)). The (002) crystal plane with a lattice fringe of 0.34 nm comprising graphic carbon with many defects were clearly observed in the carbon shell. In addition, numerous ultrasmall nanoparticles 1.5–2 nm

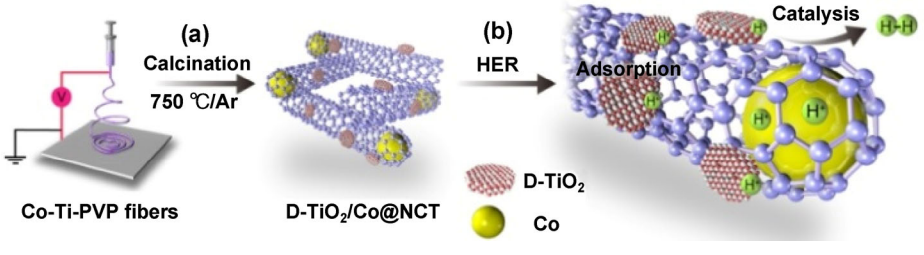

Figure 1 Schematic of the synthesis of D-TiO_2/Co@NCT and the corresponding catalytic reaction.

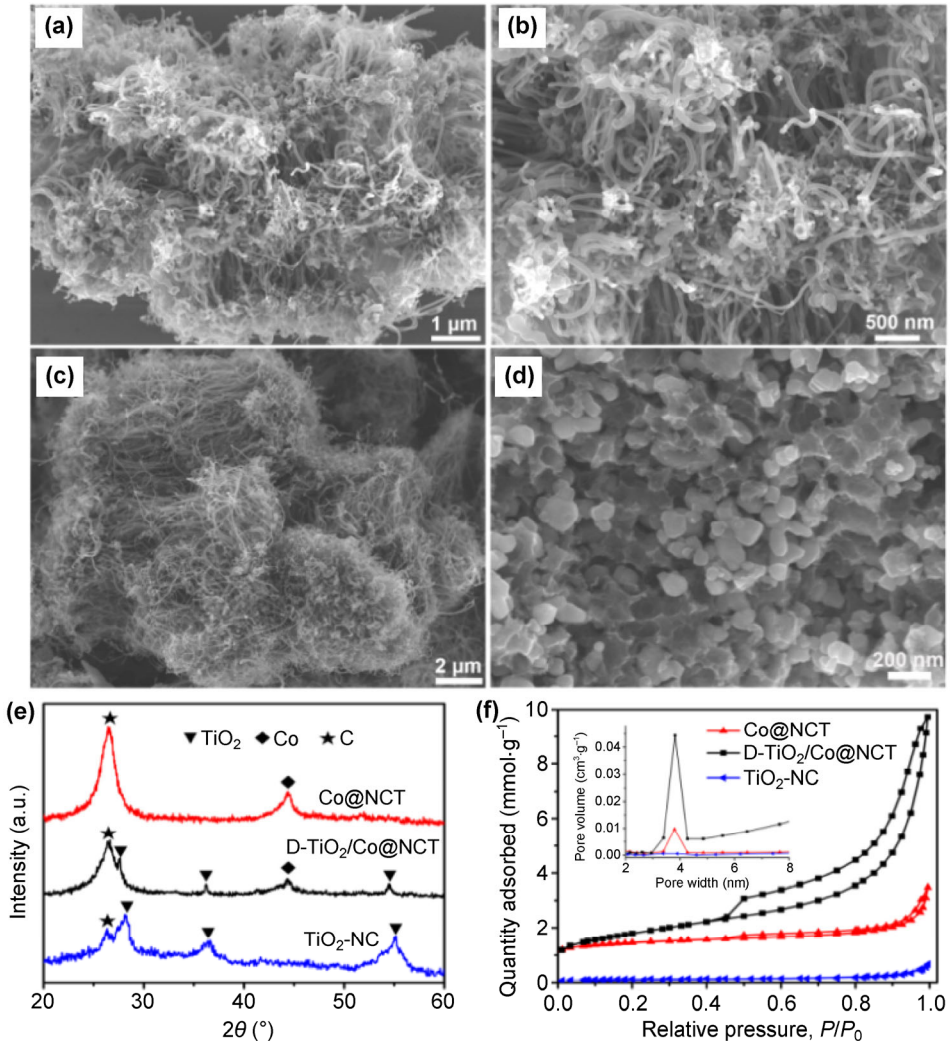

Figure 2 FESEM images (a)–(d), XRD patterns (e), and nitrogen adsorption/desorption isotherms (f) of D-TiO_2/Co@NCT (a) and (b), Co@NCT (c) and TiO_2-NC (d). The inset of (f) shows the pore-size distribution.

in size were loaded on the surface of the CNTs (Fig. 3(c) and Fig. S3 in the ESM). The product was washed by 1 M HCl overnight to remove the residual metals. Therefore, considering the previous characterization results, the ultrasmall and acid-insoluble nanoparticles on the surface of the CNTs should be TiO_2 nanoparticles. However, no crystal lattices were observed in the ultrasmall TiO_2 nanoparticles, suggesting low crystallization with a high defect density. In contrast, the TiO_2 nanoparticles in TiO_2-NC had a larger size of 20–30 nm and a lattice fringe of 0.325 nm, corresponding to the (110) plane of TiO_2 (Fig. 3(d)).

XPS was performed to determine the elemental compositions and valence states, clearly revealing the elements titanium, carbon, oxygen, cobalt, and nitrogen in the D-TiO_2/Co@NCT (Fig. S4(a) in the ESM). Deconvolution of the high-resolution scan of the metal Co 2p electrons revealed two peaks at 781.9 and 797.3 eV, which had no difference between the D-TiO_2/Co@NCT and Co@NCT (Fig. S4(b) in the ESM). As shown in Fig. 3(e), the normal valence state of Ti^{4+} with the peak at 458.9 eV was detected for both the D-TiO_2/Co@NCT and TiO_2-NC. However, the peak with a lower binding energy at 455.2 eV assigned to Ti^{3+} was only observed in the D-TiO_2/Co@NCT, indicating that the particle size determined the density of oxygen defects. The EPR spectra confirm this, indicating intrinsic defects (Fig. 3(f)). The signal at g = 2.00 is attributed to the radical O_2^-, which was generated from the reduction of O_2 adsorbed by the

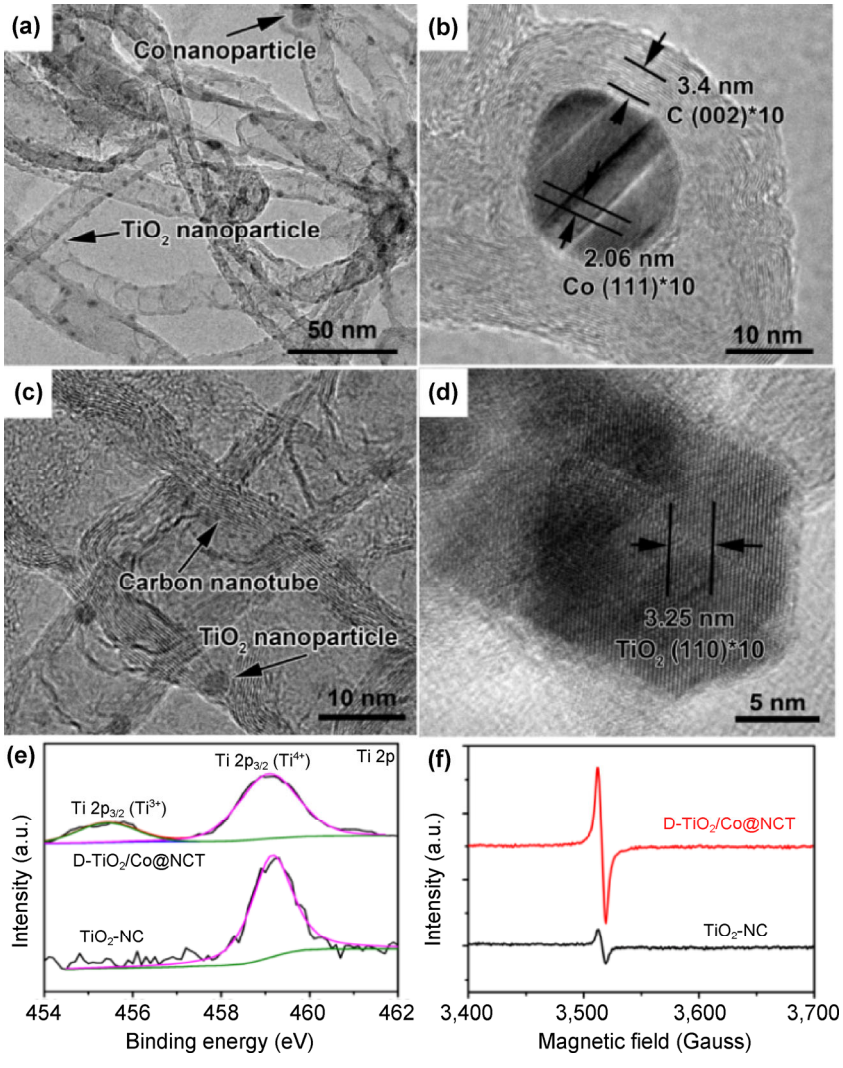

Figure 3 TEM images of (a)–(c) D-TiO_2/Co@NCT and (d) TiO_2-NC. (e) XPS and (f) EPR spectra of Ti 2p in the D-TiO_2/Co@NCT and TiO_2-NC.

surface Ti^{3+} in the defective TiO_2 [39–41]. The EPR signal for the D-TiO_2/Co@NCT was far stronger than that of TiO_2-NC, indicating the higher defect density of Ti^{3+}.

The electrocatalytic activities of the D-TiO_2/Co@NCT and blank samples including Co@NCT, TiO_2-NC, and 20 wt.% Pt/C for HER were examined by electrochemical measurements in 0.5 M H_2SO_4. As shown in Fig. 4(a), the D-TiO_2/Co@NCT had an apparent non-zero cathodic current of 1 mA·cm^{-2} at −57.5 mV vs. RHE, which was markedly lower than those of Co@NCT (−186.8 mV) and TiO_2-NC (−395 mV) but subpar compared with that of 20 wt.% Pt/C (−10 mV). In addition, as shown in Fig. 4(b) and Fig. S5 in the ESM, the Tafel slope (73.5 mV·dec^{-1}) and exchange current density (0.21 mA·cm^{-2}) of the D-TiO_2/Co@NCT were far smaller than those of Co@NCT (105.1 mV·dec^{-1}, 0.48 mA·cm^{-2}), implying a Volmer–Heyrovsky mechanism for the D-TiO_2/Co@NCT in the HER. EIS was important for directly examining the interfacial reactions and electrode kinetics in the HER. In the typical Nyquist plots obtained from the EIS response of the D-TiO_2/Co@NCT, the radius of the semicircles quickly decreased as the overpotentials increased: from 4,857 Ω·cm^{-2} at −150 mV to 1,400 Ω·cm^{-2} at −250 mV, which are far smaller than the corresponding values for Co@NCT and TiO_2-NC (Fig. S6 in the ESM). This suggests the fast electron transfer and

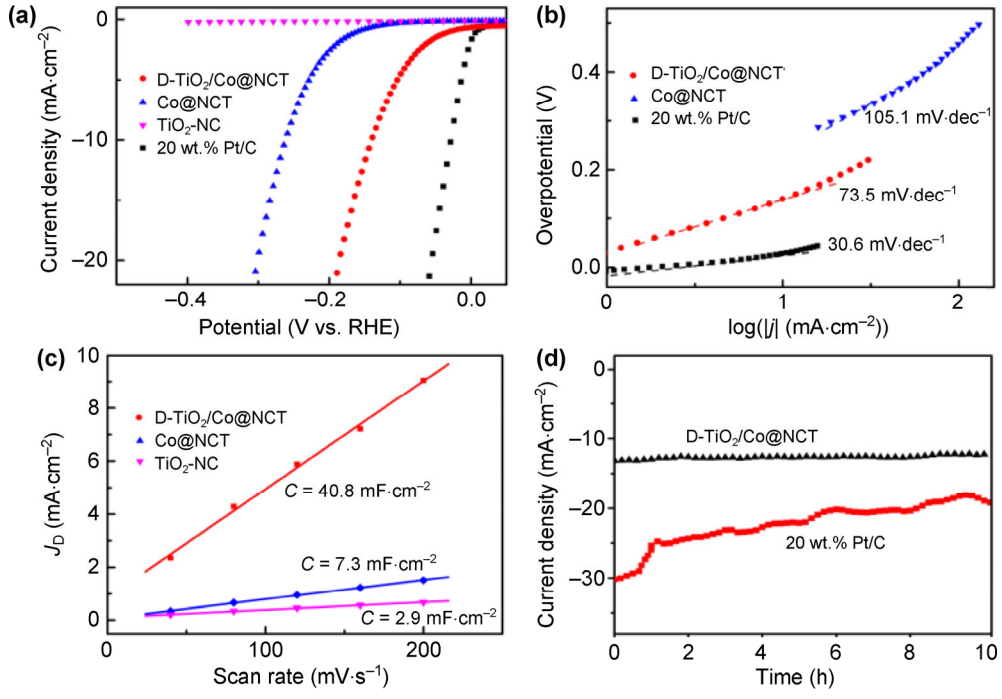

Figure 4 (a) Polarization curves for the HER in 0.5 M H_2SO_4 for a GC electrode modified with D-TiO_2/Co@NCT, Co@NCT, TiO_2-NC, and 20 wt.% Pt/C (not iR-corrected). The potential sweep rate was 5 mV·s^{-1}. (b) Corresponding Tafel plots derived from (a). (c) Double-layer charging currents at +0.05 V with respect to the potential scan rate. (d) Current–time plots of the D-TiO_2/Co@NCT and 20 wt.% Pt/C with an overpotential of 150 mV.

consequently facile HER kinetics at the electrocatalyst/electrolyte interface. The low resistance of the D-TiO_2/Co@NCT caused the small difference between the polarization curves with and without iR correction (Fig. S7 in the ESM).

CV is an effective method for estimating the electrochemically active surface area of electrodes at a solid–liquid interface (Fig. S8 in the ESM). Figure 4(c) shows that the double-layer capacitance of the D-TiO_2/Co@NCT was 40.8 mF·cm^{-2}, which was larger than those of the Co@NCT (7.3 mF·cm^{-2}) and TiO_2-NC (2.9 mF·cm^{-2}). This is consistent with the BET results (Fig. 2(f)). However, after correction according to the electrochemical area, the D-TiO_2/Co@NCT still had the smallest onset potential for the HER (Fig. S9 in the ESM), implying that the electrochemical area can only affect the catalytic current density of catalysts but not their intrinsic catalytic activity.

The practical operation was examined using a long-term hydrogen-generation experiment at a current density higher than 10 mA·cm^{-2}. Figure 4(d) shows the current–time curve of D-TiO_2/Co@NCT catalyzed over 10 h at an overpotential of 150 mV. The nearly invariant current density of 12.5 mA·cm^{-2} indicates the good catalytic durability of the D-TiO_2/Co@NCT in the acidic electrolyte and was more stable than that of the 20 wt.% Pt/C (collapsed by 32%). The current densities obtained from the *i*–*t* curve are usually lower or equal to those obtained from the polarization curve [31, 42]. The gas produced by the cathode was determined to be H_2 via gas chromatographic measurements, and the production rate was confirmed to be 1.6 μmol·h^{-1} (Fig. S10 in the ESM). Therefore, the D-TiO_2/Co@NCT had a low onset potential of −57.5 mV with a Tafel slope of 73.5 mV·dec^{-1}, a high catalytic current density (167 mV@10 mA·cm^{-2}), and high catalytic stability in 0.5 M H_2SO_4, which are better than or comparable to those of the leading carbon-based HER catalysts, such as cobalt-embedded nitrogen-rich CNTs (−140 mV, 80 mV·dec^{-1}, and 260 mV, respectively) [15], FeCo@N-doped CNTs (−70 mV, 74 mV·dec^{-1}, and 276 mV, respectively) [37], the nitrogen-doped graphene/cobalt embedded porous carbon polyhedron (−58 mV, 126 mV·dec^{-1}, and 229 mV,

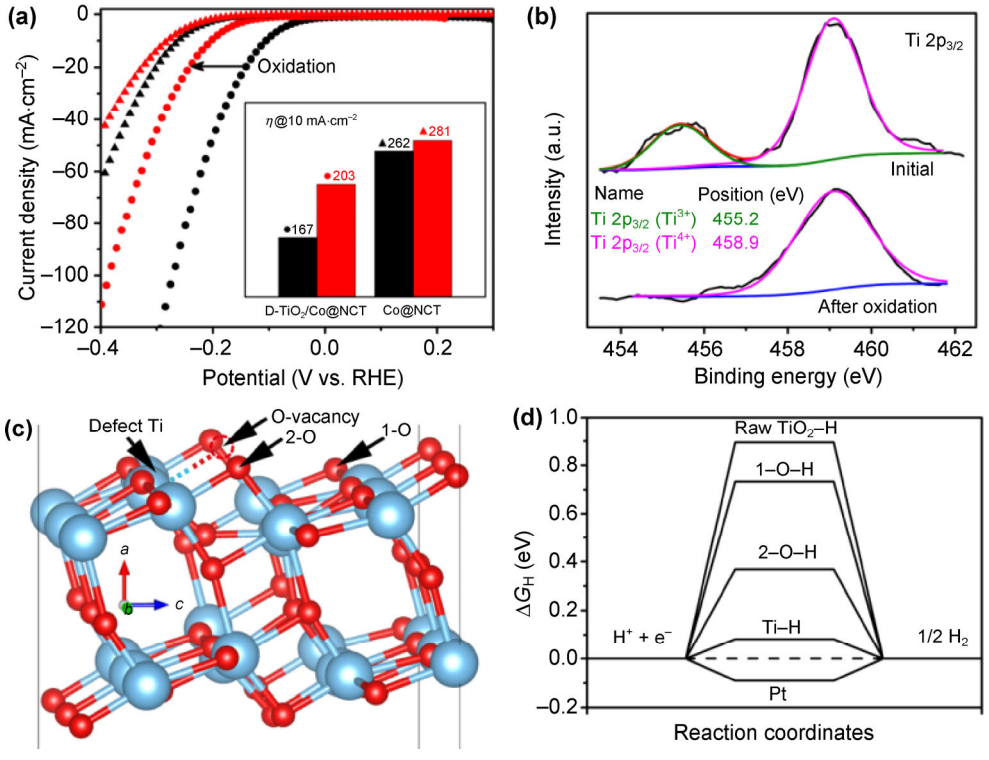

Figure 5 (a) Polarization curves of D-TiO$_2$/Co@NCT and Co@NCT before (black curves) and after (red curves) the electrochemical oxidation treatment. The inset shows the corresponding overpotential at 10 mA·cm^{-2}. (b) XPS Ti 2p spectra of D-TiO$_2$/Co@NCT before and after the electrochemical oxidation. (c) Relaxed atomic model of TiO$_2$ with one oxygen vacancy. (d) ΔG_H profile for the HER for perfect and defective TiO$_2$.

respectively) [16], and the Co–C–N complex (55 mV·dec^{-1} and 138 mV) [43], as summarized in Table S1 in the ESM. In addition, the TiO$_2$ in the D-TiO$_2$/Co@NCT is an efficient photocatalyst that can establish the photocathode for photoelectrochemical hydrogen production. As a proof of concept, a three-electrode device was used to measure the photocurrent density–potential (*J*–*E*) data in 0.5 M H_2SO_4 under irradiation from a xenon lamp (100 mW·cm^{-2}). The overpotential (vs. RHE, current density of 10 mA·cm^{-2}) of the D-TiO$_2$/Co@NCT showed an obvious decrease from darkness to light (167 to 106 mV) contributing to the semiconducting light absorber of D-TiO$_2$ (Fig. S11(a) in the ESM). In contrast, the Co@NCT showed a negligible increase in the current density under luminous radiation. This is confirmed by the Tafel-curve (Fig. S11(b) in the ESM), photocurrent (Fig. S11(c) in the ESM, efficient separation of photogenerated electron–hole pairs), and EIS (Fig. S11(d) in the ESM, fast charge transfer across the electrode/electrolyte interface) measurements.

To confirm the effect of the defect-rich structure of TiO$_2$ on the HER, D-TiO$_2$/Co@NCT were electrochemically oxidized to remove Ti^{3+} by CV in an oxidation potential range of 0 to +1.2 V vs. a saturated calomel electrode (Fig. S12 in the ESM). After the oxidation treatment, the HER activity of the D-TiO$_2$/Co@NCT was significantly degraded, and the onset potential increased from −57.5 to −150 mV vs. RHE (Fig. 5(a)). In comparison, the onset potential of Co@NCT exhibited almost no change, and only the current density slightly decreased. XPS confirmed that the low valence of Ti^{3+} disappeared after the electrochemical oxidation of the D-TiO$_2$/Co@NCT (Fig. 5(b)). However, cobalt also had zero valence (Fig. S13 in the ESM) owing to the protection of the carbon shell. These findings suggest that the oxygen vacancies in the D-TiO$_2$ were the main reason for the enhanced HER activity [39]. In addition, the synergetic effect among the cobalt core, nitrogen-doped carbon shell, and D-TiO$_2$ played an important role in enhancing the HER activity. In the catalytic reaction, by doping

the metal core with nitrogen, the electronic state density of carbon can be modulated to produce additional active sites [19]. Regarding the structural regulation, the CNTs are crucial for synthesizing the ultrasmall TiO_2 nanoparticles in D-TiO_2/Co@NCT.

To understand the effect of oxygen vacancies on the HER reactivity, DFT calculations were performed for a 2 × 3 × 4 TiO_2 supercell with one oxygen vacancy (Fig. 5(c) and Fig. S14 in the ESM). When the oxygen vacancy was introduced, the ΔG_H on the defect titanium atom, O-1 atom, and O-2 atom were calculated. ΔG_H is used as a descriptor for the HER catalytic activity and depends on the geometric and electronic structures of the catalyst [18]. For a highly active HER catalyst, ΔG_H is closer to 0 eV, indicating that hydrogen is bound neither too strongly nor too weakly. As shown in Fig. 5(d), perfect TiO_2 has a large ΔG_H of 0.895 eV. When an oxygen vacancy is introduced, the ΔG_H of the defect titanium, O-1, and O-2 atoms in D-TiO_2 are effectively changed to 0.081, 0.732, and 0.368 eV, respectively. Among the various sites, the defect titanium site had the smallest ΔG_H of 0.081 eV, which is comparable to that of the platinum catalyst (ΔG_H = −0.09 eV). The DFT calculations reveal that the oxygen vacancies allowed hydrogen to directly bind to the exposed titanium atoms, which were new catalytic sites for the HER.

4 Conclusions

We presented an electrospinning-calcination method for preparing D-TiO_2/Co@NCT as an efficient HER electrocatalyst with a low onset potential of −57.5 mV (1 mA·cm^{-2}), a small Tafel slope of 73.5 mV·dec^{-1}, and extraordinary long-term durability. Regarding the structural regulation, the CNTs were crucial for synthesizing the ultrasmall TiO_2 nanoparticles in the D-TiO_2/Co@NCT. In the catalytic reaction, the ultrasmall TiO_2 nanoparticles with a defect-rich environment improved the catalytic activity of the D-TiO_2/Co@NCT. XPS, EPR spectroscopy, and theoretical calculations confirmed that the oxygen vacancies in the ultrasmall TiO_2 nanoparticles introduced new catalytic sites of Ti^{3+} and reduced the hydrogen-adsorption free energy. This remarkable improvement in the catalytic activity rendered by the defect-rich environment introduces a promising method for regulating hydrogen-production activity.

Acknowledgements

We thank the Fundamental Research Funds for the Central Universities (No. D2153880), Project of Public Interest Research and Capacity Building of Guangdong Province (No. 2014A010106005) and the National Natural Science Foundation of China (No. 51502096).

Electronic Supplementary Material: Supplementary material (cyclic voltammograms, polarization curves, Nyquist plots and the equivalent circuit, SEM images, XPS spectra, and DFT calculations) is available in the online version of this article at http://dx.doi.org/10.1007/s12274-017-1462-1.

References

[1] Sathre, R.; Scown, C. D.; Morrow, W. R., III; Stevens, J. C.; Sharp, I. D.; Ager, J. W., III; Walczak, K.; Houle, F. A.; Greenblatt, J. B. Life-cycle net energy assessment of large-scale hydrogen production via photoelectrochemical water splitting. *Energy Environ. Sci.* **2014**, *7*, 3264–3278.

[2] Ye, G. L.; Gong, Y. J.; Lin, J. H.; Li, B.; He, Y. M.; Pantelides, S. T.; Zhou, W.; Vajtai, R.; Ajayan, P. M. Defects engineered monolayer MoS_2 for improved hydrogen evolution reaction. *Nano Lett.* **2016**, *16*, 1097–1103.

[3] Sun, C. C.; Dong, Q. C.; Yang, J.; Dai, Z. Y.; Lin, J. J.; Chen, P.; Huang, W.; Dong, X. C. Metal–organic framework derived $CoSe_2$ nanoparticles anchored on carbon fibers as bifunctional electrocatalysts for efficient overall water splitting. *Nano Res.* **2016**, *9*, 2234–2243.

[4] Bai, S.; Wang, C. M.; Deng, M. S.; Gong, M.; Bai, Y.; Jiang, J.; Xiong, Y. J. Surface polarization matters: Enhancing the hydrogen-evolution reaction by shrinking Pt shells in Pt-Pd-graphene stack structures. *Angew. Chem., Int. Ed.* **2014**, *53*, 12120–12124.

[5] Wang, C. H.; Hu, F.; Yang, H. C.; Zhang, Y. J.; Lu, H.; Wang, Q. B. 1.82 wt.% Pt/N, P co-doped carbon overwhelms 20 wt.% Pt/C as a high-efficiency electrocatalyst for hydrogen evolution reaction. *Nano Res.* **2017**, *10*, 238–246.

[6] Konkena, B.; Junge Puring, K.; Sinev, I.; Piontek, S.; Khavryuchenko, O.; Durholt, J. P.; Schmid, R.; Tüysüz, H.; Muhler, M.; Schuhmann, W. et al. Pentlandite rocks as sustainable and stable efficient electrocatalysts for hydrogen generation. *Nat. Commun.* **2016**, *7*, 12269.

[7] Wu, H. B.; Xia, B. Y.; Yu, L.; Yu, X. Y.; Lou, X. W. Porous molybdenum carbide nano-octahedrons synthesized via confined carburization in metal-organic frameworks for efficient hydrogen production. *Nat. Commun.* **2015**, *6*, 6512.

[8] Wang, D. Y.; Gong, M.; Chou, H. L.; Pan, C. J.; Chen, H. A.; Wu, Y. P.; Lin, M. C.; Guan, M.; Yang, J.; Chen, C. W. et al. Highly active and stable hybrid catalyst of cobalt-doped FeS_2 nanosheets-carbon nanotubes for hydrogen evolution reaction. *J. Am. Chem. Soc.* **2015**, *137*, 1587–1592.

[9] Zhang, X. W.; Meng, F.; Mao, S.; Ding, Q.; Shearer, M. J.; Faber, M. S.; Chen, J. H.; Hamers, R. J.; Jin, S. Amorphous MoS_xCl_y electrocatalyst supported by vertical graphene for efficient electrochemical and photoelectrochemical hydrogen generation. *Energy Environ. Sci.* **2015**, *8*, 862–868.

[10] Yang, L. J.; Zhou, W. J.; Lu, J.; Hou, D. M.; Ke, Y. T.; Li, G. Q.; Tang, Z. H.; Kang, X. W.; Chen, S. W. Hierarchical spheres constructed by defect-rich MoS_2/carbon nanosheets for efficient electrocatalytic hydrogen evolution. *Nano Energy* **2016**, *22*, 490–498.

[11] Ye, W.; Ren, C. H.; Liu, D. B.; Wang, C. M.; Zhang, N.; Yan, W. S.; Song, L.; Xiong, Y. J. Maneuvering charge polarization and transport in 2H-MoS_2 for enhanced electrocatalytic hydrogen evolution reaction. *Nano Res.* **2016**, *9*, 2662–2671.

[12] Wang, S. Y.; Zhang, L.; Li, X.; Li, C. L.; Zhang, R. J.; Zhang, Y. J.; Zhu, H. W. Sponge-like nickel phosphide–carbon nanotube hybrid electrodes for efficient hydrogen evolution over a wide pH range. *Nano Res.***2017**, *10*, 415–425.

[13] Tian, J. Q.; Liu, Q.; Asiri, A. M.; Sun, X. P. Self-supported nanoporous cobalt phosphide nanowire arrays: An efficient 3D hydrogen-evolving cathode over the wide range of pH 0–14. *J. Am. Chem. Soc.* **2014**, *136*, 7587–7590.

[14] Li, Y. J.; Zhang, H. C.; Jiang, M.; Kuang, Y.; Sun, X. M.; Duan, X. Ternary NiCoP nanosheet arrays: An excellent bifunctional catalyst for alkaline overall water splitting. *Nano Res.* **2016**, *9*, 2251–2259.

[15] Zou, X. X.; Huang, X. X.; Goswami, A.; Silva, R.; Sathe, B. R.; Mikmeková, E.; Asefa, T. Cobalt-embedded nitrogen-rich carbon nanotubes efficiently catalyze hydrogen evolution reaction at all pH values. *Angew. Chem., Int. Ed.* **2014**, *53*, 4372–4376.

[16] Zhou, W. J.; Zhou, J.; Zhou, Y. C.; Lu, J.; Zhou, K.; Yang, L. J.; Tang, Z. H.; Li, L. G.; Chen, S. W. N-doped carbon-wrapped cobalt nanoparticles on N-doped graphene nanosheets for high-efficiency hydrogen production. *Chem. Mater.* **2015**, *27*, 2026–2032.

[17] Tahir, M.; Mahmood, N.; Zhang, X. X.; Mahmood, T.; Butt, F. K.; Aslam, I.; Tanveer, M.; Idrees, F.; Khalid, S.; Shakir, I. et al. Bifunctional catalysts of Co_3O_4@GCN tubular nanostructured (TNS) hybrids for oxygen and hydrogen evolution reactions. *Nano Res.* **2015**, *8*, 3725–3736.

[18] Deng, J.; Ren, P. J.; Deng, D. H.; Bao, X. H. Enhanced electron penetration through an ultrathin graphene layer for highly efficient catalysis of the hydrogen evolution reaction. *Angew. Chem., Int. Ed.* **2015**, *54*, 2100–2104.

[19] Zhou, W. J.; Yin, Z. Y.; Du, Y. P.; Huang, X.; Zeng, Z. Y.; Fan, Z. X.; Liu, H.; Wang, J. Y.; Zhang, H. Synthesis of few-layer MoS_2 nanosheet-coated TiO_2 nanobelt hetero-structures for enhanced photocatalytic activities. *Small* **2013**, *9*, 140–147.

[20] Liu, B.; Liu, L.-M.; Lang, X.-F.; Wang, H.-Y.; Lou, X. W.; Aydil, E. S. Doping high-surface-area mesoporous TiO_2 microspheres with carbonate for visible light hydrogen production. *Energy Environ. Sci.* **2014**, *7*, 2592–2597.

[21] Li, L. D.; Yan, J. Q.; Wang, T.; Zhao, Z. J.; Zhang, J.; Gong, J. L.; Guan, N. J. Sub-10 nm rutile titanium dioxide nanoparticles for efficient visible-light-driven photocatalytic hydrogen production. *Nat. Commun.* **2015**, *6*, 5881.

[22] Liu, P. X.; Zhao, Y.; Qin, R. X.; Mo, S. G.; Chen, G. X.; Gu, L.; Chevrier, D. M.; Zhang, P.; Guo, Q.; Zang, D. D. et al. Photochemical route for synthesizing atomically dispersed palladium catalysts. *Science* **2016**, *352*, 797–800.

[23] Kuld, S.; Thorhauge, M.; Falsig, H.; Elkjær, C. F.; Helveg, S.; Chorkendorff, I.; Sehested, J. Quantifying the promotion of Cu catalysts by ZnO for methanol synthesis. *Science* **2016**, *352*, 969–974.

[24] Bruix, A.; Rodriguez, J. A.; Ramírez, P. J.; Senanayake, S. D.; Evans, J.; Park, J. B.; Stacchiola, D.; Liu, P.; Hrbek, J.; Illas, F. A new type of strong metal-support interaction and the production of H_2 through the transformation of water on Pt/CeO_2(111) and Pt/CeO_x/TiO_2(110) catalysts. *J. Am. Chem. Soc.* **2012**, *134*, 8968–8974.

[25] Xu, Y. F.; Zhang, C.; Zhang, L. X.; Zhang, X. H.; Yao, H. L.; Shi, J. L. Pd-catalyzed instant hydrogenation of TiO_2 with enhanced photocatalytic performance. *Energy Environ. Sci.* **2016**, *9*, 2410–2417.

[26] Chen, X. B.; Liu, L.; Yu, P. Y.; Mao, S. S. Increasing solar absorption for photocatalysis with black hydrogenated titanium dioxide nanocrystals. *Science* **2011**, *331*, 746–750.

[27] Pei, D.-N.; Gong, L.; Zhang, A.-Y.; Zhang, X.; Chen, J.-J.; Mu, Y.; Yu, H.-Q. Defective titanium dioxide single crystals exposed by high-energy {001} facets for efficient oxygen reduction. *Nat. Commun.* **2015**, *6*, 8696.

[28] An, L.; Yan, H. J.; Chen, X.; Li, B.; Xia, Z. H.; Xia, D. G. Catalytic performance and mechanism of N-CoTi@$CoTiO_3$ catalysts for oxygen reduction reaction. *Nano Energy* **2016**, *20*, 134–143.

[29] Swaminathan, J.; Subbiah, R.; Singaram, V. Defect-rich metallic titania ($TiO_{1.23}$)—An efficient hydrogen evolution catalyst for electrochemical water splitting. *ACS Catal.* **2016**, *6*, 2222–2229.

[30] Yin, Y.; Han, J. C.; Zhang, Y. M.; Zhang, X. H.; Xu, P.; Yuan, Q.; Samad, L.; Wang, X. J.; Wang, Y.; Zhang, Z. H. et al. Contributions of phase, sulfur vacancies, and edges to the hydrogen evolution reaction catalytic activity of porous molybdenum disulfide nanosheets. *J. Am. Chem. Soc.* **2016**, *138*, 7965–7972.

[31] Zhou, W. J.; Lu, J.; Zhou, K.; Yang, L. J.; Ke, Y. T.; Tang, Z. H.; Chen, S. W. $CoSe_2$ nanoparticles embedded defective carbon nanotubes derived from MOFs as efficient electrocatalyst for hydrogen evolution reaction. *Nano Energy* **2016**, *28*, 143–150.

[32] Xie, J. F.; Zhang, J. J.; Li, S.; Grote, F.; Zhang, X. D.; Zhang, H.; Wang, R. X.; Lei, Y.; Pan, B. C.; Xie, Y. Controllable disorder engineering in oxygen-incorporated MoS_2 ultrathin nanosheets for efficient hydrogen evolution. *J. Am. Chem. Soc.* **2013**, *135*, 17881–17888.

[33] Kresse, G.; Furthmüller, J. Efficiency of *ab-initio* total energy calculations for metals and semiconductors using a plane-wave basis set. *Comp. Mater. Sci.* **1996**, *6*, 15–50.

[34] Perdew, J. P.; Burke, K.; Ernzerhof, M. Generalized gradient approximation made simple. *Phys. Rev. Lett.* **1996**, *77*, 3865–3868.

[35] Kresse, G.; Joubert, D. From ultrasoft pseudopotentials to the projector augmented-wave method. *Phys. Rev. B* **1999**, *59*, 1758–1775.

[36] Nørskov, J. K.; Bligaard, T.; Logadottir, A.; Kitchin, J. R.; Chen, J. G.; Pandelov, S.; Stimming, U. Trends in the exchange current for hydrogen evolution. *J. Electrochem. Soc.* **2005**, *152*, J23–J26.

[37] Deng, J.; Ren, P. J.; Deng, D. H.; Yu, L.; Yang, F.; Bao, X. H. Highly active and durable non-precious-metal catalysts encapsulated in carbon nanotubes for hydrogen evolution reaction. *Energy Environ. Sci.* **2014**, *7*, 1919–1923.

[38] Xia, B. Y.; Yan, Y.; Li, N.; Wu, H. B.; Lou, X. W.; Wang, X. A metal–organic framework-derived bifunctional oxygen electrocatalyst. *Nat. Energy* **2016**, *1*, 15006.

[39] Wu, Q. P.; Huang, F.; Zhao, M. S.; Xu, J.; Zhou, J. C.; Wang, Y. D. Ultra-small yellow defective TiO_2 nanoparticles for co-catalyst free photocatalytic hydrogen production. *Nano Energy* **2016**, *24*, 63–71.

[40] Zuo, F.; Wang, L.; Wu, T.; Zhang, Z. Y.; Borchardt, D.; Feng, P. Y. Self-doped Ti^{3+} enhanced photocatalyst for hydrogen production under visible light. *J. Am. Chem. Soc.* **2010**, *132*, 11856–11857.

[41] Zuo, F.; Bozhilov, K.; Dillon, R. J.; Wang, L.; Smith, P.; Zhao, X.; Bardeen, C.; Feng, P. Y. Active facets on titanium(III)-doped TiO_2: An effective strategy to improve the visible-light photocatalytic activity. *Angew. Chem., Int. Ed.* **2012**, *51*, 6223–6226.

[42] Zhou, W. J.; Xiong, T. L.; Shi, C. H.; Zhou, J.; Zhou, K.; Zhu, N. W.; Li, L. G.; Tang, Z. H.; Chen, S. W. Bioreduction of precious metals by microorganism: Efficient gold@N-doped carbon electrocatalysts for the hydrogen evolution reaction. *Angew. Chem., Int. Ed.* **2016**, *55*, 8416–8420.

[43] Wang, Z.-L.; Hao, X.-F.; Jiang, Z.; Sun, X.-P.; Xu, D.; Wang, J.; Zhong, H.-X.; Meng, F.-L.; Zhang, X.-B. C and N hybrid coordination derived Co–C–N complex as a highly efficient electrocatalyst for hydrogen evolution reaction. *J. Am. Chem. Soc.* **2015**, *137*, 15070–15073.